The Iranian Journal of Mechanical Engineering Transactions of ISME
Journal homepage: https://jmee.isme.ir/
Vol. 25, No. 2, 2024, pp. 40-62

Research Paper

DOI: https://doi.org/10.30506/jmee.2024.1990806.1313

A Hybrid Contactless Air-magnetic Bearing System for Operating at 15,000 rpm

Hossein Barati[*]
M.Sc.

Mohammad Reza Karafi[†]
Assistant Professor

This paper introduces a Hybrid Air-Magnetic bearing for a two-pole three-phase induction motor. In high-speed machine, contact bearings are not usable. As a result, utilizing non-contact bearings are alternative. Magnetic and air bearings are non-contact types that can be employed independently or together. This study employed a combination of magnetic and air bearings. At first, the system suspended the motor shaft by using air bearings. Then the Magnetic bearings damp the system's vibrations at high speeds. This Hybrid Air-Magnetic bearing system significantly reduces control and calculation efforts while improving stability, robustness, and reliability at high speeds. The air bearing is used with an air gap of 6 μm and a pressure of 7 bars. Resistance between the shaft and air bearing housing was measured to be 0 in the non-suspended condition, 5 $M\Omega$ in the suspended condition at zero speed, and 43 $M\Omega$ at 15,000 rpm. At 15,000 rpm, the motor vibrated with an amplitude of 2 μm. The greatest observed acceleration amplitude is 4.5, 4.3, 3.5, and 3.3 m/s2 at 3900, 6900, 10200, and 13800 rpm, respectively.

Keywords: Magnetic bearing, Air bearing, Hybrid, High speed

1 Introduction

Today's sophisticated industries require high rotating speeds. Such speeds are commonly utilized in the medical and defense industries, aircraft, aviation engine test stands, gas turbines, motors, compressors, and centrifuges. Ball bearings have long been employed in low-rotational speeds. At high speeds, ball bearings are constrained by friction, wear, and substantial heat losses. Contactless magnetic bearings are a viable alternative.

---

[*] M.Sc., Department of Mechanical Engineering, Tarbiat Modares University, Tehran, Iran, hossein.barati@modares.ac.ir

[†] Corresponding author, Assistant Professor, Department of Mechanical Engineering, Tarbiat Modares University, Tehran, Iran, Karafi@modares.ac.ir

Received: 2023/03/13, Revised: 2024/05/18, Accepted: 2024/06/12

They have been used in a wide range of sectors in recent decades. But magnetic suspension systems in sensitive applications such as aviation engines, power plant turbines, and centrifuges require high reliability, stability, and crash prevention [1-10]. As a result, researchers have been particularly interested in hybrid systems for improving suspension reliability and stability. The combination of air and magnetic bearings improves system reliability, robustness, and stability while reducing vibrations [11-15].

The literature can be divided into three categories: (1) study on air bearings and their aerostatic and aerodynamic effects; (2) research on magnetic bearings and their control mechanisms; and (3) research on hybrid air-magnetic bearings. Zhao et al. [16] proposed an analytical model for the optimal design of air bearings, focusing on air bearings built using porous carbon technology. Gao et al. [17] investigated at the aerostatic and aerodynamic impacts of radial air bearings in ultrafast spindle motors. Because of the eccentricity of the rotor and stator, the aerodynamic effect of air bearings increased with eccentricity, allowing for higher loadings. Wu et al. [18] studied mechatronic design of spindle motors and concluded that the rotor and air bearings should be treated as an integrated system at high speeds, and the electrical motor and servo control should be simultaneously designed in the mechanical structure. They measured stiffness versus air gap and reported that the stiffness was maximized at an air gap of 12 μm. Smirnov et al. [19] studied high-speed machines using active magnetic bearings they optimize such machines using changes in the rotor and bearing structures. Yamamoto et al. [20] evaluated shaft suspension system through a combination of three bearings. They used a passive magnetic bearing and an electrodynamic bearing (eddy current) for radial suspension and an active magnetic bearing to control the shaft in the axial direction. They reported radial and axial rotor displacement with and without the electrodynamic bearing at rotational speeds of up to 1900 rpm. Zhihang Huang et al. [21] begin by categorizing various magnetic bearings and conducting a thorough analysis of their qualities and characteristics, with an emphasis on magnetic circuit structures. They also discuss how control methods affect magnetic bearing performance. Modern control theory has proven a 50% improvement in position accuracy and adjustment time over classic PID control. Heshmat et al. [22] pioneered the use of a combination of air and magnetic bearings in a rotor with a diameter of 150 mm for gas turbines. This study employed aerodynamic air bearings. Jang et al. [23] investigated the combination of air bearing with an active magnetic bearing to improve high speed instability. This study employed aerostatic air bearings while a thrust active magnetic bearing is located at one end of the rotor. Qing et al. [24] had an overview about hybrid gas Magnetic Bearings and provided a comprehensive survey about different types of combination of gas bearings and magnetic bearings.

In this paper, magnetic and air bearings are combined to achieve rotational speeds greater than 15,000 rpm. At zero speed, an aerostatic air bearing uses external pump pressure to provide suspension, and at greater speeds, a magnetic bearing is used to reduce radial vibrations. The magnetic bearing forces are calculated using analytical equations, whereas the air bearing is simulated with Comsol software. The experimental setup was evaluated by monitoring vibrations and system performance at various speeds. The magnetic bearing's performance in the presence of an air bearing is characterized by system control and vibration damping.

2 Analytical modeling of magnetic bearings

As the rotor speeded up, shaft's position is measured using sensors in the radial direction and control by the magnetic bearing and controller. In general, electromagnetic force on the rotor Figure (1) is written as [25]:

$$F = \frac{B^2 A}{2\mu_0}(2\cos\alpha) \tag{1}$$

$$F = \frac{\varphi^2}{\mu_0 A}(\cos\alpha) \tag{2}$$

where F is the electromagnetic force on the rotor (N), A is the air gap cross-sectional area (m^2), B is the magnetic flux density in the air gap (T), μ_0 is the magnetic permeability of air (Hm^{-1}), and φ is the magnetic flux (Wb).
In a magnetic circuit,

$$\varphi = \frac{\mathcal{F}}{\mathcal{R}} \tag{3}$$

where $\mathscr{F}$ is the magnetomotive force (A), and $\mathcal{R}$ denotes magnetic reluctance (A/Wb). By inserting the values of $\mathscr{F}$ and $\mathscr{R}$ in equation (3), the following relationship is obtained:

$$\varphi = \frac{Ni}{\left(\frac{2g}{\mu_0} + \frac{l_{fe}}{\mu_0 \mu_r A_{fe}}\right)} \tag{4}$$

where N is the number of turns, i denotes the coil current (A), g denotes the air gap (m), L_{fe} is the average magnetic path length in the iron core (m), A_{fe} is the core cross-sectional area of the air gap (m^2), and μ_r represents the relative magnetic permeability of iron. The insertion of Eq. (4) in Eq. (2) yields:

$$F = \frac{N^2 i^2}{\left(\frac{2g}{\mu_0} + \frac{l_{fe}}{\mu_0 \mu_r A_{fe}}\right){}^{\wedge}2} \frac{\cos\propto}{\mu_0 A} \tag{5}$$

$$F = \frac{\cos\propto}{1 + \frac{l_{fe} A}{2 g \mu_r A_{fe}}} \frac{N^2 A \mu_0}{4} \frac{i^2}{g^2} \tag{6}$$

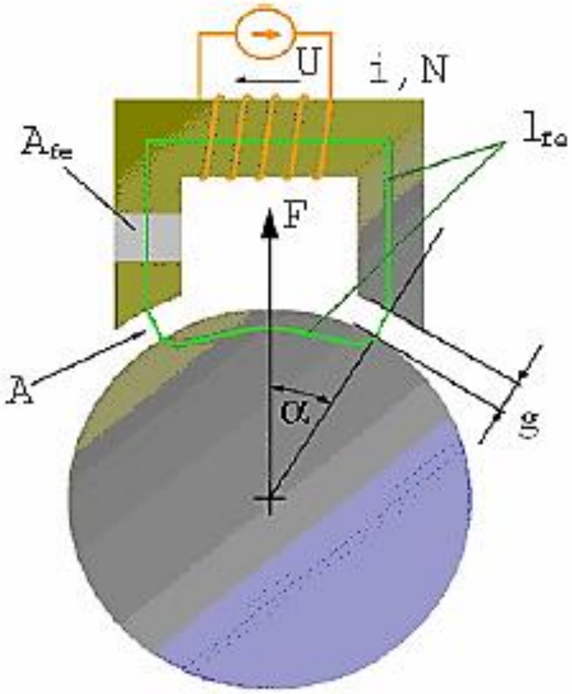

Figure 1 Magnetic circuit of a magnetic bearing

Here, K is defined as:

$$K = \frac{\cos\propto}{1+\frac{l_{fe}A}{2\,g\mu_r A_{fe}}}\frac{N^2 A\mu_0}{4} \tag{7}$$

Therefore, Eq. (7) can be rewritten as:

$$F = K\frac{i^2}{g^2} \tag{8}$$

A pair of facing magnetic coils is typically employed in active magnetic bearings, and Eq. (8) can be rewritten as:

$$F_i = K\frac{\left(I_0+i_{control_i}\right)^2}{(x_i-g)^2} - K\frac{\left(I_0-i_{control_i}\right)^2}{(x_i+g)^2} \tag{9}$$

where I_0 is the base current, and $i_{control_i}$ is the control current. Thus, x_i and $i_{control_i}$ are zero when the shaft is suspended at the center. Based on Eq. (9), it can be said that the force is nonlinear regarding to the current and space. Linearization around an operating point is an approach to design a controller for this system. As the rotor is placed in the center of the system using the air bearings, the displacement of the rotor around the center is very small. This simplifies the design of a controller for the magnetic bearing to a great extent.

3 Numerical simulation of the air and magnetic bearings

In this section, numerical simulations of air bearings and magnetic bearings were performed in COMSOL software to get the dimensions and sizes of the components required for the setup, as well as the forces acting on them.

3.1 Air bearing simulat

A 3D model of the air bearing is generated in COMSOL V.5.2. Solid Mechanics and Creep Flow Physics are used in this analysis. The analysis is done under steady-state conditions and the effect of Inertia is neglected. Normal meshes are use in this simulation. Figure (2) illustrates the three-dimensional air bearing model. It should be noted that in the designed air bearing, the air inlet hole is located one side, so it cannot be modeled as an axisymmetric problem.

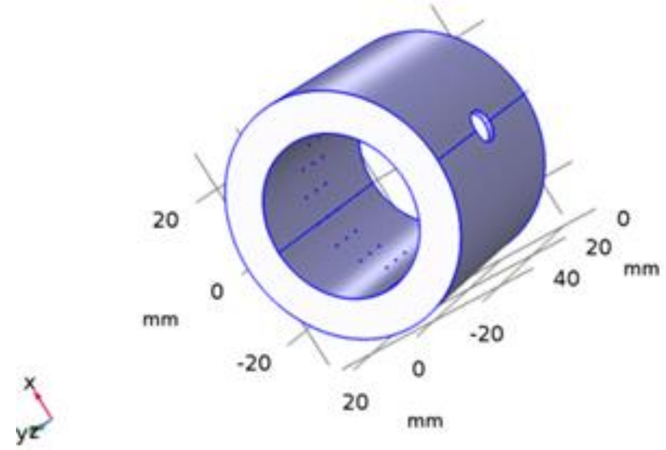

Figure 2 3D air bearing model in the COMSOL software

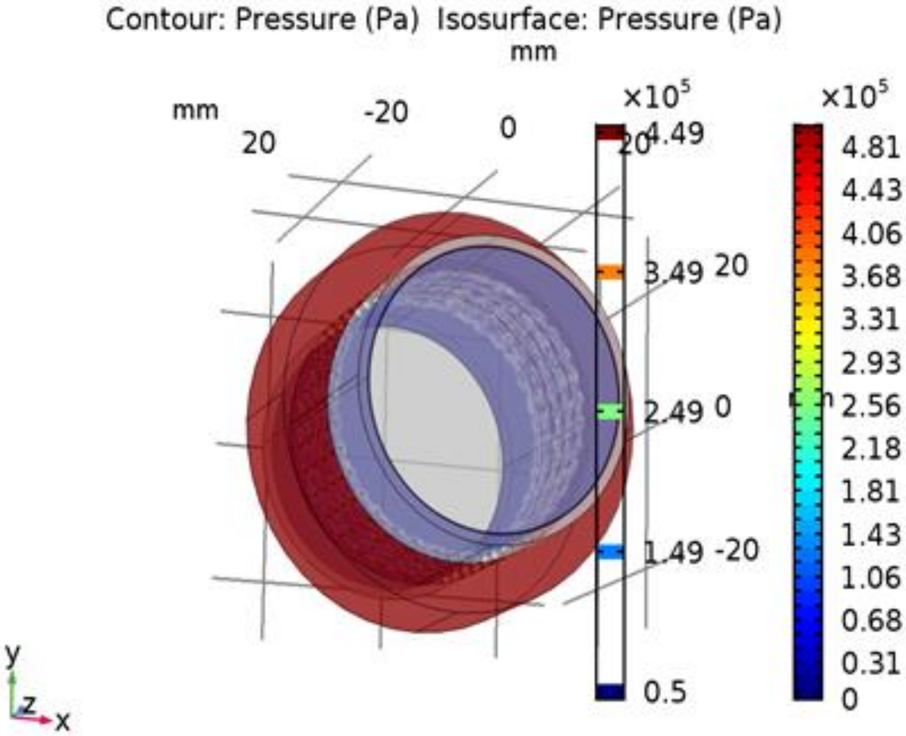

Figure 3 Contour: Pressure (Pa) Streamline: Velocity field Isosurface: Pressure (Pa)

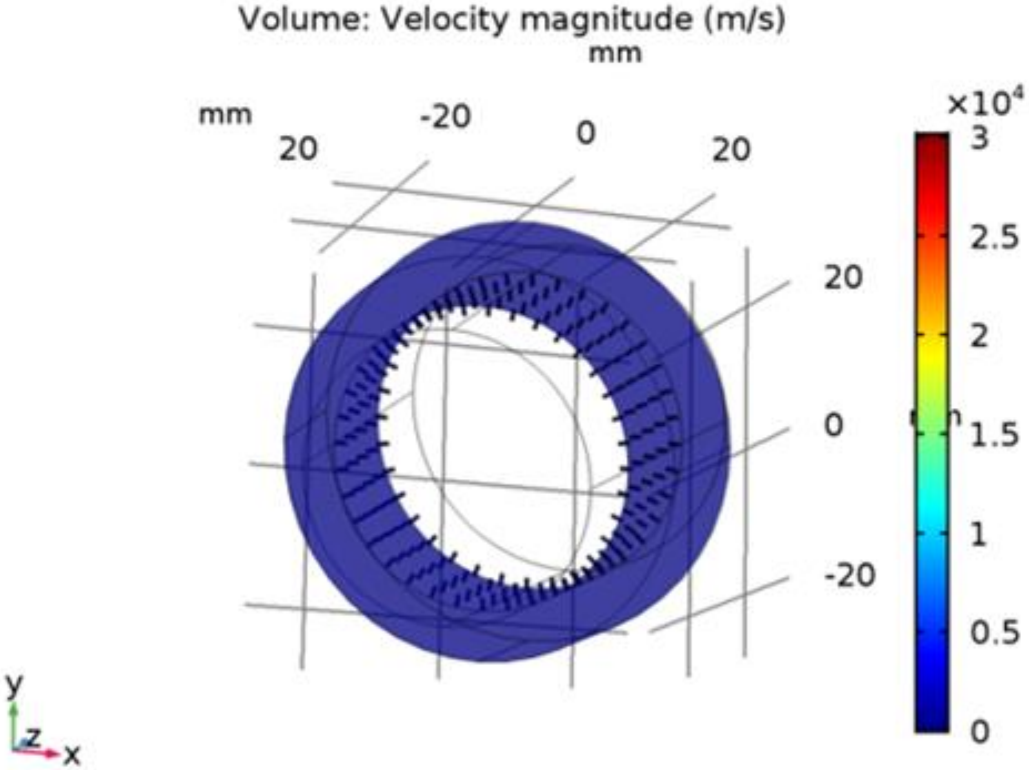

Figure 4 Fluid velocity (m/s)

Table 1 Force on the shaft at different air gaps

Force (N) h=500micron	Force (N) h=200micron	Force (N) h=150micron
10.57	25.99	33.19

The air gap is considered as moving meshes. Figure (3) represents the pressure contours. Figure (4) depicts the fluid velocities in the inlet and outlet of the air tank. The pressure contours were obtained for an air bearing with an air gap of 500 μm and five rows of pores, each with 36 holes of a diameter of 0.25 mm. The input pressure was set to 5 bars.

Table (1) provides the force on the shaft at different air gaps for an input pressure of 5 bars. The numerical simulations were carried out in a steady state. Also, air leakage, pressure drop along the channel, and pressure drop through the pores were neglected. Therefore, experimental tests were employed to obtain the realistic performance of the air bearing.

3.2 Magnetic bearing simulation

Four symmetric coils were employed in a double-facing-coil configuration within the core of the magnetic bearing, as shown in Figure (5).

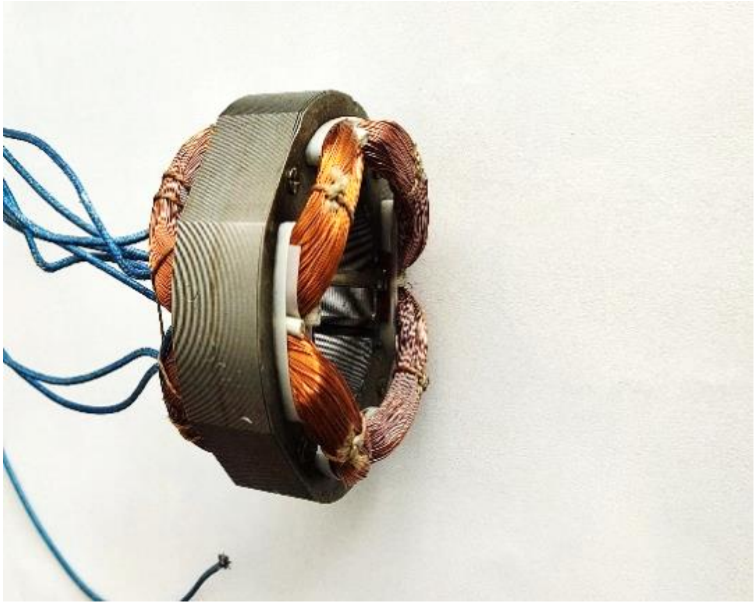

Figure 5 Magnetic bearing stator

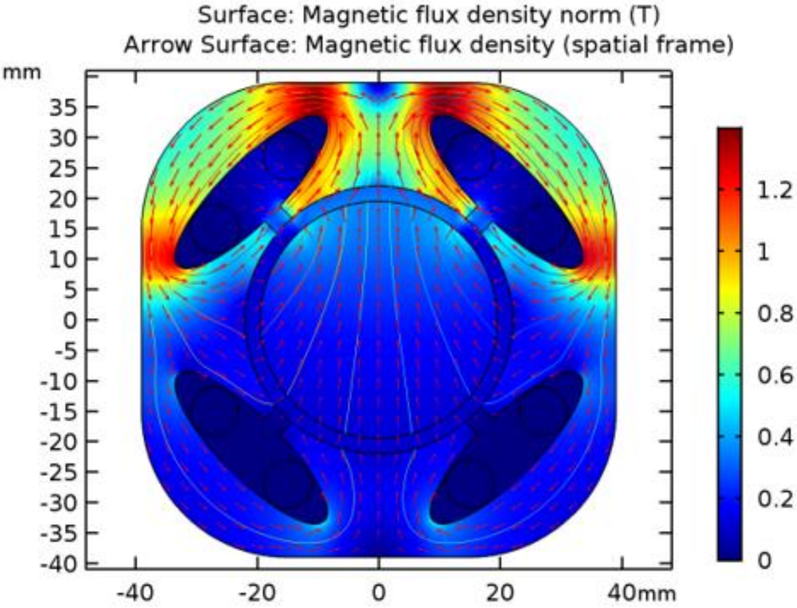

Figure 6 Magnetic flux density distribution of the core (T)

Table 2 Electromagnetic force on the shaft

Electromagnetic force, y component (N), I_f=1.2A	Electromagnetic force, y component (N), I_f=1A	Electromagnetic force, y component (N), I_f=0.8A	Electromagnetic force, y component (N), I_f=0.6A
28.081	20.161	13.029	7.3380

The core was simulated two-dimensionally in COMSOL in Magnetic Field Physics under a steady-state condition via normal meshes. The laminated core had a thickness of 25 mm, with 800 turns and a wire thickness of 0.30 mm. The shaft and inner magnetic bearing diameters were 39 and 42 mm, respectively. Figure (6) illustrates the magnetic flux density distribution with the excitation of a single (top) coil using a current of 1.2 A.

Table (2) reports the force on the shaft at different excitation currents.

As can be seen, the force was maximized at an excitation current of 1.2A before saturation of the core, which is satisfactory for the rotor weight.

3.3 Natural frequencies of the shaft

The natural frequencies of the rotor are important at high speeds. They can be obtained via numerical simulations. In this way, the rotor model in Solid Works was imported to COMSOL, and the rotor material was introduced. The shaft was made up of ASTM 4140 steel (MO40), while the bushes were made from iron. Modal analysis was carried out in Solid Mechanics physics to obtain the natural frequencies, as reported in Table (3). Figure (7) depicts the first flexural mode of the shaft at 331.55 Hz.

According to Table (3), the natural frequencies of the shaft are higher than 331 Hz. Thus, the shaft could rotate without mechanical resonance below 331 Hz.

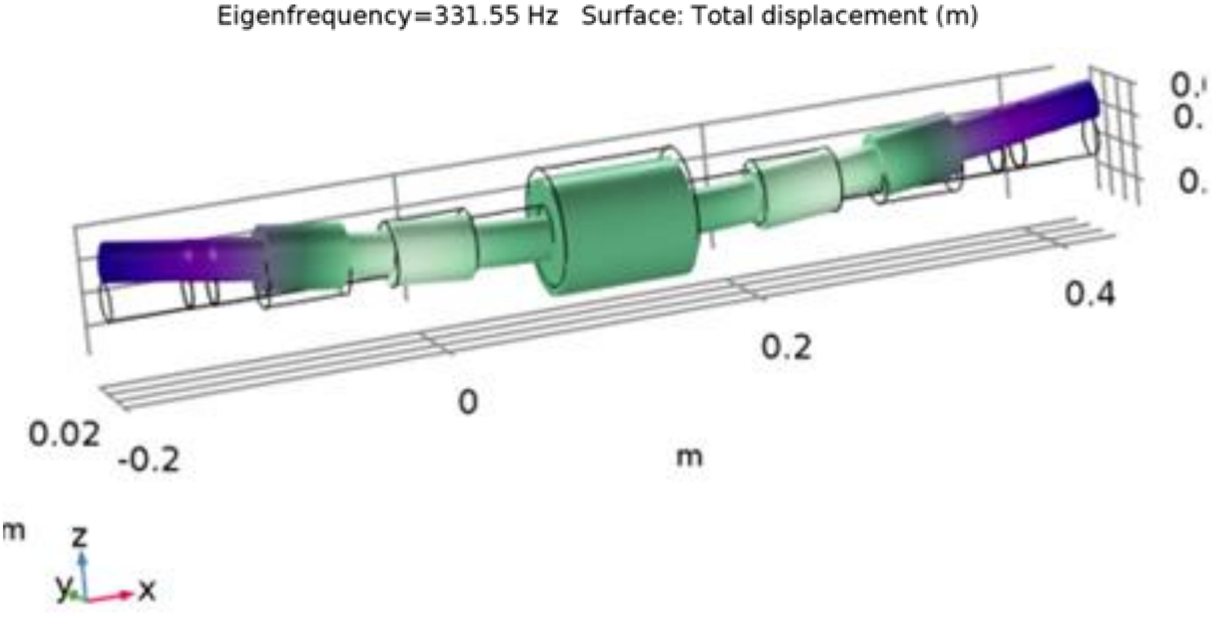

Figure 7 The first natural flexural mode of the shaft at 331.55 Hz

Table 3 Natural frequencies of the shaft

Mode	1	2	3	4	5	6
Frequency (Hz)	331.32	860.62	1629	2278	2443	2743

3.4 Analytical versus numerical models

Table 4 Comparison of Analytical and numerical magnetic forces in the magnetic bearing

Parameter	Excitation Current (A)	Analytical Model	Numerical Model	Error (%)
Magnetic force on the shaft (N) applied by the top coil at an air gap of 1.5 mm	0.6	8.17	7.33	10
	0.8	14.36	13.02	9
	1	22.14	20.16	9
	1.2	31.65	28.05	11

Table (4) compares the analytical and numerical magnetic forces of the magnetic bearing. As can be seen, in the Table (4), the analytical and numerical error is about 10%. This error is due to the fact that in the analytical calculations, the core is considered to be made of iron, but in the numerical simulation, the core is considered to be laminated, and the effect of the saturation of the core is also considered.

4 Experimental setup and tests

A number of earlier works employed the motor on one side [22, 23, 26]. In such circumstances, the shaft is attached to the driver (electric motor or turbine) by a coupling and is not suspended on one side. This connection generates vibration, limiting the speed. To overcome this challenge, Induction motor as the driver was placed in the middle and the shaft being suspended on both sides, as shown in Figure (8). However, it is difficult to place the shaft at the same center as the motor and the hybrid bearing system. Thus, the final experimental setup was altered, as shown in Figure (9). The air bearings were seated on the motor structure. As a result, the rotor was placed at the center of the motor, and some small adjustments were required, which would be implemented using fillers. In this section, the specifications and features of the various components used in this setup are explained. Also, the parts that needed to be designed and fabricated are reported in detail.

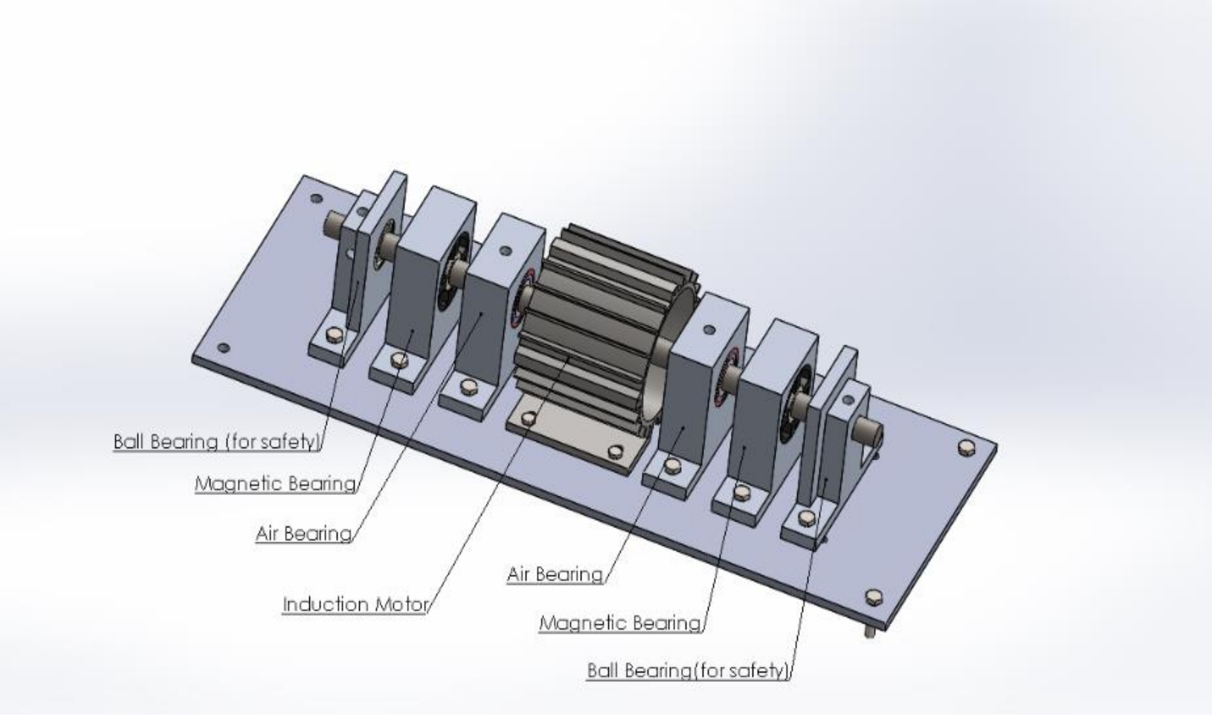

Figure 8 Schematic of the hybrid air-magnetic bearing system

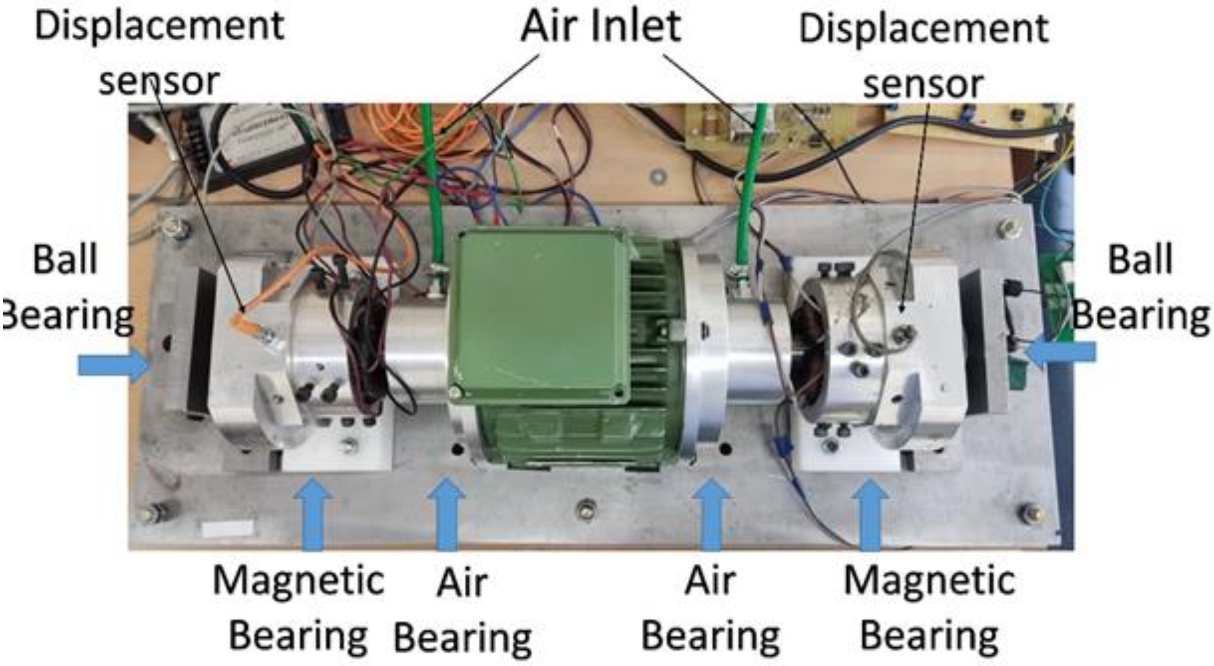

Figure 9 Final experimental setup

4.1 Electromotor selection

A 1.5kW two pole induction motor was employed, as shown in Figure (10). Motors of more poles could be used in practice; however, the motor speed declines as the number of poles rises, requiring higher frequencies to achieve higher speeds. For example, a 4-pole induction motor has a speed of 1500 rpm at 50 Hz, and an excitation frequency of 666 Hz is required to raise the speed to 20,000 rpm. This frequency is not in the frequency range of commercial Variable Frequency Drive (VFD). The maximum frequency of commercial VFDs is 400 Hz.

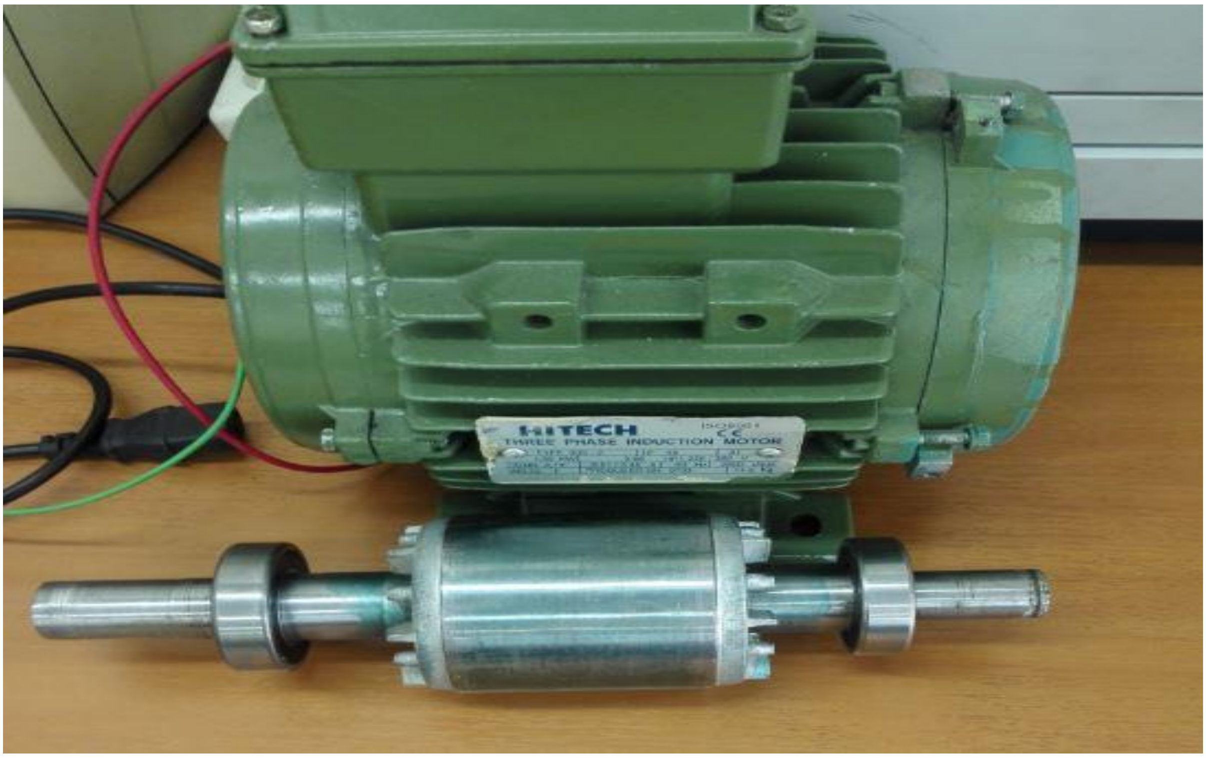

Figure 10 A 1.5kW three-phase induction motor and its dismantled rotor

4.2 *Rotor modifications*

The motor shaft is modified to implement in the air-magnetic bearing system. The moment of inertia, natural frequencies, and balancing are important parameters in shaft design. Figure (11) illustrates the final model of the shaft, while Figure (12) depicts the fabricated shaft on the air bearing seat. The squirrel-cage rotor was separated from the original shaft and pressed onto the new shaft of a new material and size. The shaft was made up of MO40 steel and was fabricated in a stepped form with a tolerance of ±0.01 mm using a CNC machine. The bushes were pressed. Ball bearings seats are provided at the end of the shaft. Ball bearings are used to ensure the system safety in the case of contactless bearing failure. Furthermore, the shaft was dynamically balanced at 20,000 rpm using Schenck DH2 balancing machine manufactured in Germany. The shaft had a weight of 5.700 kg, and its moment of inertia was calculated to be 2.06 kgm^2.

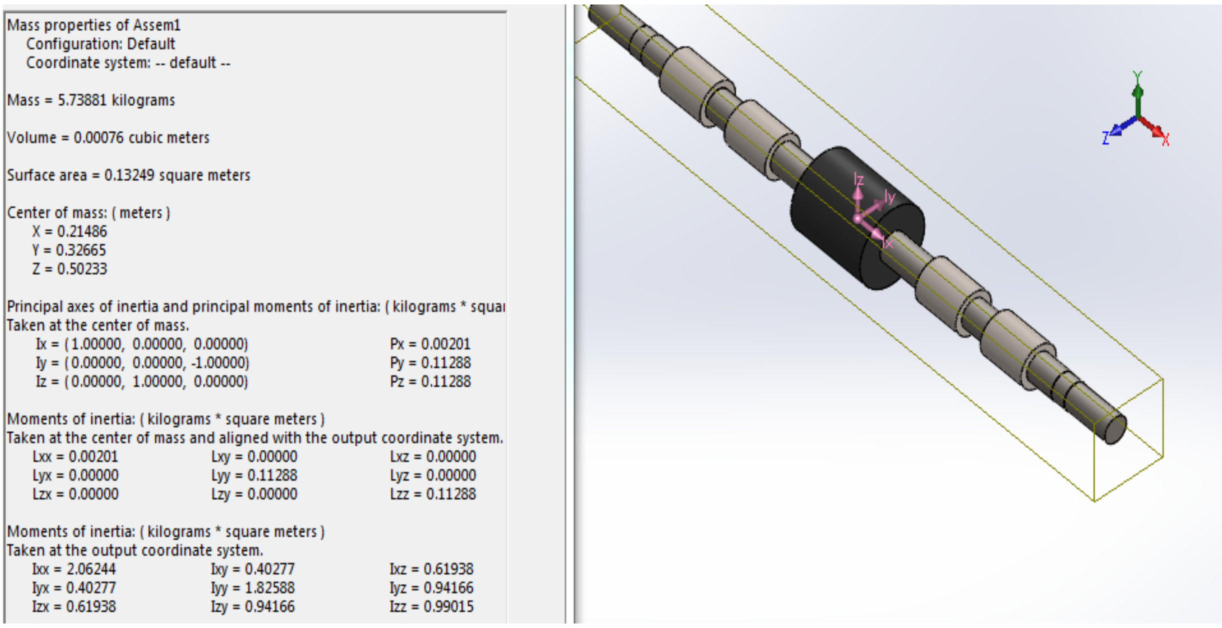

```
Mass properties of Assem1
    Configuration: Default
    Coordinate system: -- default --

Mass = 5.73881 kilograms

Volume = 0.00076 cubic meters

Surface area = 0.13249 square meters

Center of mass: ( meters )
     X = 0.21486
     Y = 0.32665
     Z = 0.50233

Principal axes of inertia and principal moments of inertia: ( kilograms * squa
Taken at the center of mass.
      Ix = ( 1.00000,  0.00000,  0.00000)                Px = 0.00201
      Iy = ( 0.00000,  0.00000, -1.00000)                Py = 0.11288
      Iz = ( 0.00000,  1.00000,  0.00000)                Pz = 0.11288

Moments of inertia: ( kilograms * square meters )
Taken at the center of mass and aligned with the output coordinate system.
     Lxx = 0.00201          Lxy = 0.00000          Lxz = 0.00000
     Lyx = 0.00000          Lyy = 0.11288          Lyz = 0.00000
     Lzx = 0.00000          Lzy = 0.00000          Lzz = 0.11288

Moments of inertia: ( kilograms * square meters )
Taken at the output coordinate system.
     Ixx = 2.06244          Ixy = 0.40277          Ixz = 0.61938
     Iyx = 0.40277          Iyy = 1.82588          Iyz = 0.94166
     Izx = 0.61938          Izy = 0.94166          Izz = 0.99015
```

Figure 11 Rotor model in Solid Works

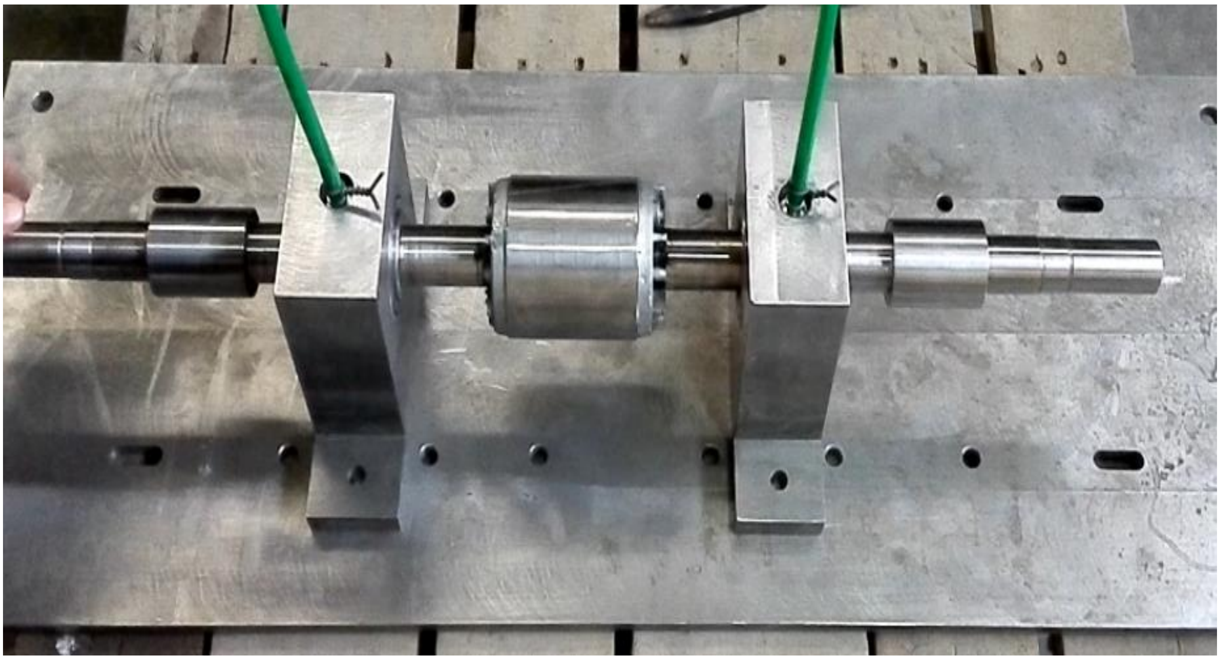

Figure 12 Fabricated rotor on the air bearing seat

4.3 Air bearing fabrication

The process of manufacturing air bearings is complex and difficult. Three different types of air bearings were created and fabricated in order to get the intended outcome. Based on the simulation's results, the initial design was created. In this design, the bearing carrier was fabricated as an external component, placing the porous piece into the bearing carrier using O-rings. This design consisted of three main components, i.e. the porous piece, carrier, and seat, along with O-rings, as shown in Figure (13). However, with this design, due to the tiny capacity of the air reservoir and the considerable air gap between the shaft and the porous piece (150 microns), the air bearing could not produce enough force to suspend the shaft. Here the O-rings had a thickness of 2 mm and an outer diameter of 42 mm.

For the second design, the bearing carrier was eliminated, and the outer diameter of the porous piece was increased to enlarge the air reservoir, as shown in Figure (14). Furthermore, the seat functioned as the bearing carrier. This design consisted of two main components, i.e., the porous piece and seat, along with O-rings. Here the O-rings had a thickness of 2 mm and an outer diameter of 52 mm. Aligning the electric motor, air bearings, magnetic bearings, and ball bearings (as shown in Figure (8)) is a difficult task, and even the slightest movement causes the parts to be misaligned.

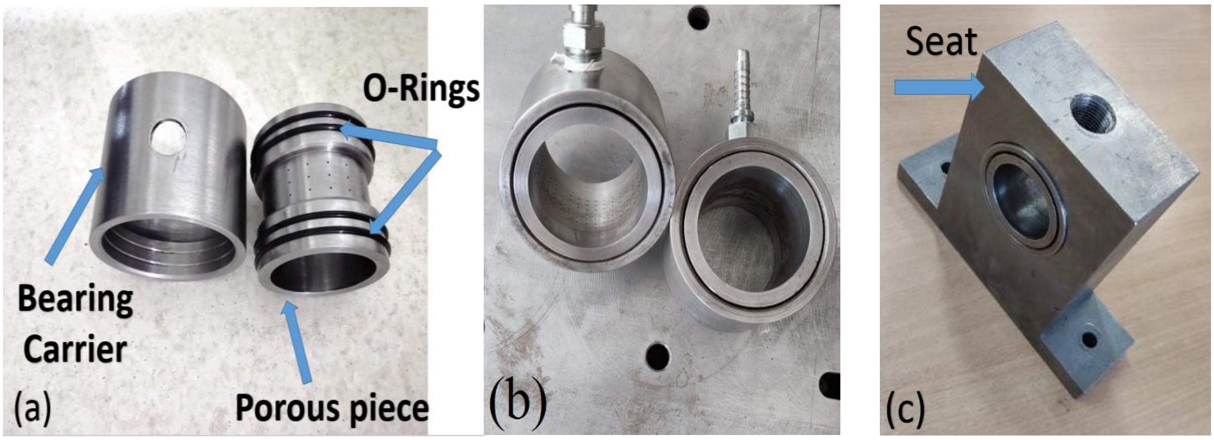

Figure 13 Schematic of the first air bearing design (**a**) before assembly, (**b**) after the assembly of the porous piece into the bearing carrier, and (**c**) after the assembly of the components into the seat

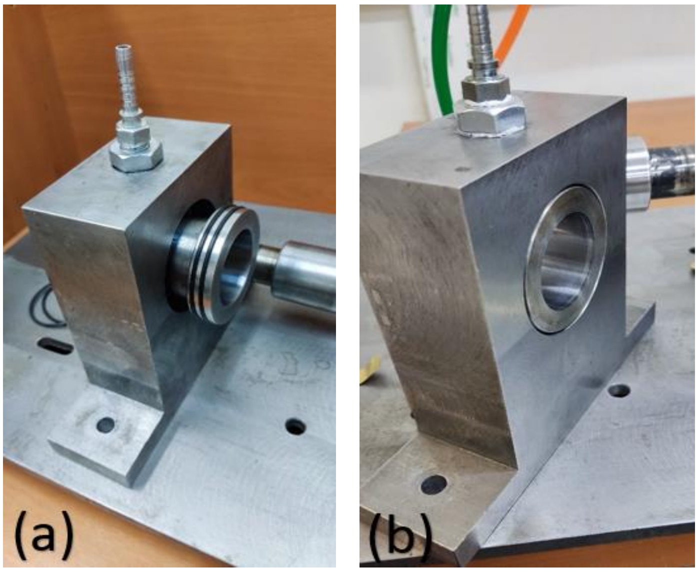

Figure 14 Schematic of the second air bearing design (**a**) before and (**b**) after assembly

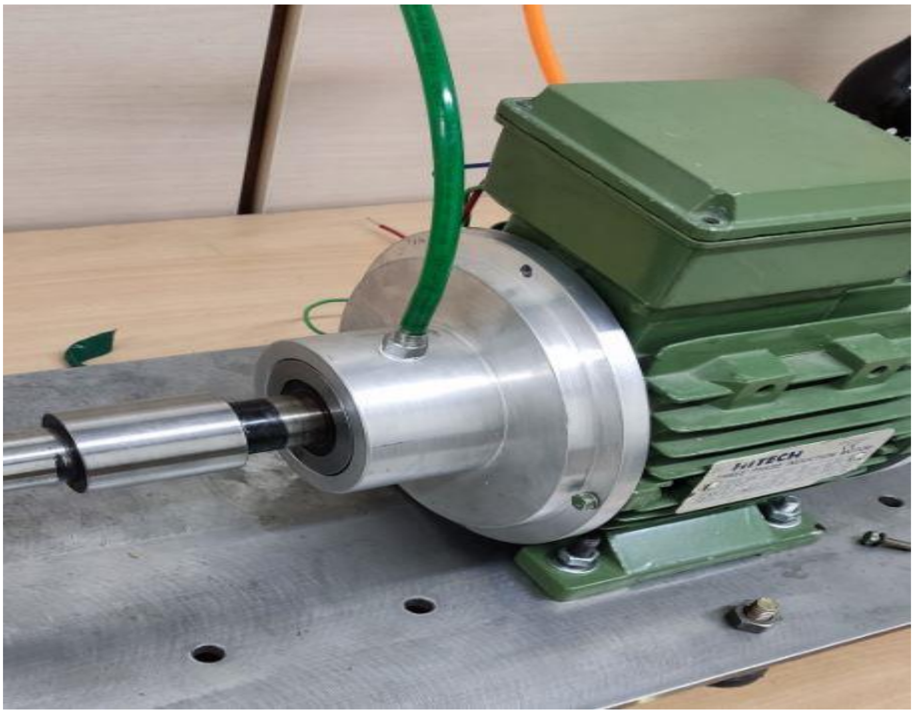

Figure 15 Schematic of the third design, the porous piece within the aluminum cap

Table 5 Comparison of the three air bearing designs

Types of air bearing design	Specification
First design	+Design based on simulation results - Small air reservoir - large air gap between the shaft and the porous piece - Insufficient force for suspension
Second design	+ Suitable air reservoir + enough air gap between the shaft and porous piece + Sufficient force for suspension -Difficult alignment
Third design	+ Suitable air reservoir + enough air gap between the shaft and porous piece + Sufficient force for suspension +Easy alignment

For the third design, the iron seat that had been designed separately was removed, and an aluminum seat was designed to be placed on the electromotor construction, with the porous piece and O-ring inside. Figure (15) depicts the third design in which the porous piece was placed in the aluminum carrier and assembled on the motor's structure. This design consisted of two main components, i.e., the porous piece and an aluminum carrier/seat, along with O-rings.

Because the seat of the air bearing is installed on the motor frame, component alignment become much easier, and this design is chosen as the final design. Table (5) summarizes the comparisons between the three types of designs.

The fabrication of components in the third air bearing design is explained in the next two subsections.

4.3.1 Porous piece

The porous piece is a major component of air bearings and it is shown in Figure (16). It is fabricated using a CNC machine with a tolerance of ±0.01 mm for outer diameters and ±1 μm for inner diameter. It involved a total of 24 pores in two rows with an angle of 30 degrees and a diameter of 0.2 mm. The inner surface is grinded with a precision of 1 μm to obtain uniform surface roughness. The gap between the shaft and the porous piece of the air bearing is set to 6 μm.

4.3.2 Air bearing carrier

The bearing carrier was designed such that it would be completely sealed by O-rings after assembling on the porous piece, as shown in Figure (13b). The trapped air was discharged through the pores onto the shaft, creating an air cushion. In addition, a hole is embedded as an air inlet.

In the second design, the bearing carrier is eliminated to increase the air reservoir capacity, homogenize the air outflow through the pores and avoid rotor contact to the air bearing. Then, the seat functioned as the carrier (Figure (14)). It should be noted that the concentricity of the shaft with the motor and air bearing seat is a major challenge while assembling and testing the experimental setup due to the very small air gap (i.e. 6 μm from each side). Due to the eccentricity, shaft rotation may lead to crash and damage of the air bearing. To fix the problem and place the rotor at the same center as the stator and air bearings, the third air bearing design was employed. As the motor's structure and the stator had the same center, therefore, a specific cap was designed for the right and left sides of the motor in Solid Works, as shown in Figure (17). Finally, the aluminum air bearing's caps were fabricated using a CNC machine with a tolerance of ±0.01 mm. Figure (15) depicts the placement of the porous piece of the air bearing within the motor cap. Thus, the motor cap served as not only the air bearing seat but also the bearing carrier and con-centralized the rotor and stator.

The concentricity of the shaft and bearings declines in practice due to poor assembly precision. The sealing O-rings between the porous piece and air bearing carrier (motor cap) are an explanation. To tackle this challenge, fillers with a thickness of 50 μm are employed.

Figure 16 Porous piece of the air bearing with two rows of pores with a diameter of 0.2 mm

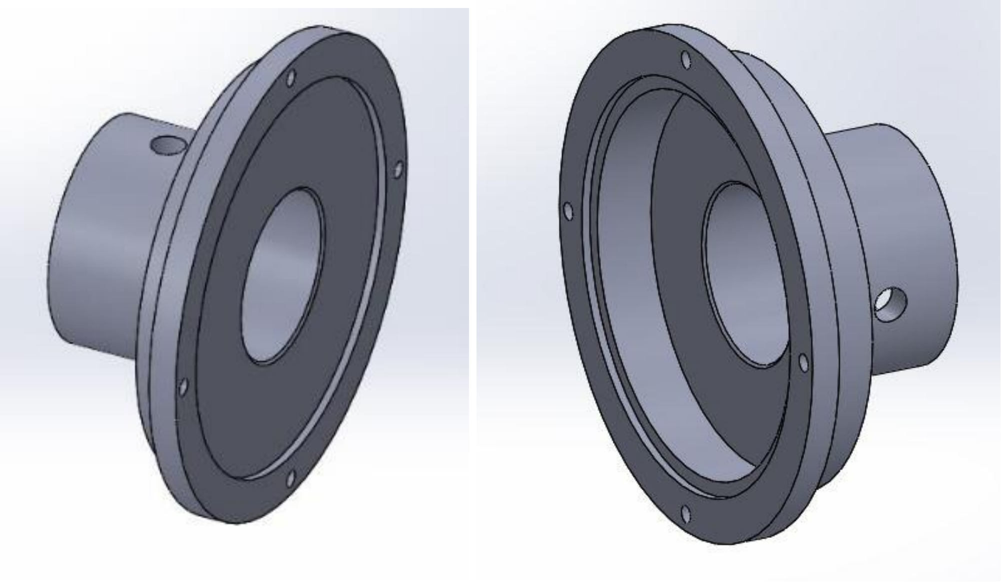

Figure 17 Aluminum cap designed for the right and left sides of the motor

4.4 Magnetic bearing

The magnetic bearing has four poles, and each pair of coils in front of each other operate together by using a current driver and an inductive gap sensor. If the motor's shaft is off-center, the position of the shaft is aligned. Magnetic bearing’s inner core diameter is 42 mm, outer core diameter is 78 mm, core thickness is 25 mm, total coil turns are 800, and a wire thickness is 0.30 mm, as shown in Figure (18). The core was placed in an aluminum seat on which sensors could be installed around it. A polytetrafluoroethylene (PTFE) stand was fabricated for the magnetic bearing to con-centralize it with the experimental setup.

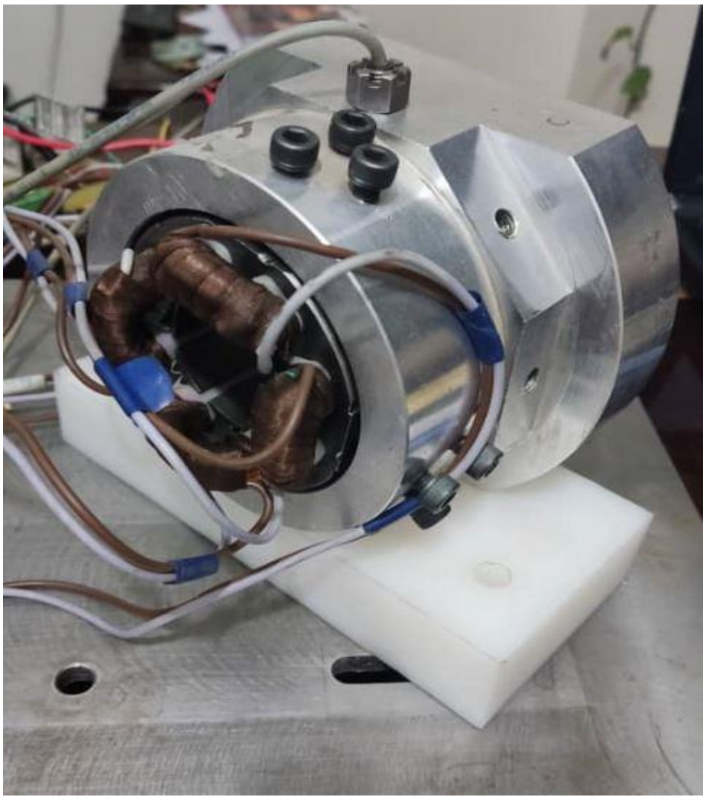

Figure 18 Magnetic bearing with a PTFE stand

4.5 Sensors

Two Contrinex inductive sensors (DW-AD-509-M8-390) are employed in each magnetic bearing to measure and control displacement of the shaft using the controller. They measure distances of 0-4 mm and have an output voltage of 0-10 V. There would be a 25 mV/µm change in the output voltage of the sensors when they are used in the linear area. A sensor is employed for each facing pair of coils, and the output of the sensor is compared to a reference voltage (5 V). An output voltage exceeding 5 V would represent a shaft displacement from the center toward the opposite coil, and an output voltage dropping below 5 V would indicate shaft displacement toward the corresponding coil. Using a controller and a current driver, the coils keep the shaft at the center. It should be noted that the shaft is initially suspended by the air bearings, and the sensors had a distance of 2 mm from the shaft, with the output sensor and error being 5 V and 0, respectively. As the shaft speed increased, the magnetic bearing damps possible radial vibration through the control system.

4.6 Driver of the coils

Figure (19) depicts the current driver for coils. The current driver and controller are responsible for keeping the shaft in the center. In this circuit, when V_{i1} (the controller's output) becomes positive, the shaft is away from the center, and coil L1 should be magnetized and pull the shaft towards itself until V_{i1}becomes zero; when V_{i1}becomes negative, the shaft is away from the center in opposite direction. In this case, coil L2 must be magnetized to pull the shaft towards itself, restoring V_{i1} to zero and placing the shaft in the center.

When V_{i1} is positive, Op-amp 1's output is positive, and transistors Q1 and Q3 are turned on, with the controlled current flowing into the coil 1, the excited coil pulls the shaft. When $V_{i1}$is negative, Op-amp 3 reverses it, and the output of Op-amp 2 becomes positive, causing transistors Q2 and Q4 turn on. With the controlled current flowing into coil 2, the excited coil pulls the shaft. The feed voltage for power transistors is +60 V. It should be noted that the 1-ohm resistor connected to the emitters of power transistors Q3 and Q4 should be of high power (5Watt). Because when the motor shaft is out of center, the current which flows through the coils passes through this resistor. If the resistor power is insufficient, it will burn.

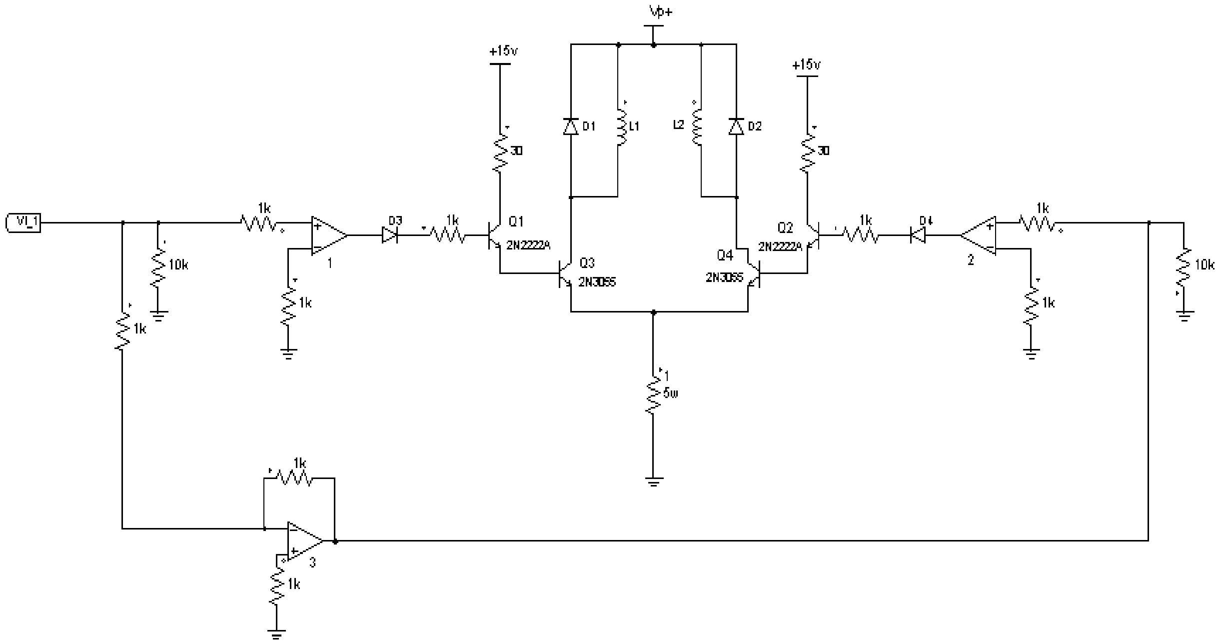

Figure 19 Current driver for a pair of facing magnetic coils

4.7 *Controller circuit*

Magnetic bearings are inherently unstable due to its transfer function (equation (9)). Therefore, it should be stabilized using a controller. The controller could be a classical lead-lag controller or a Proportional–Integral–Derivative (PID) controller. The present work adopted a Proportional-Integral (PI) controller since suspension would be initially carried out by the air bearings.

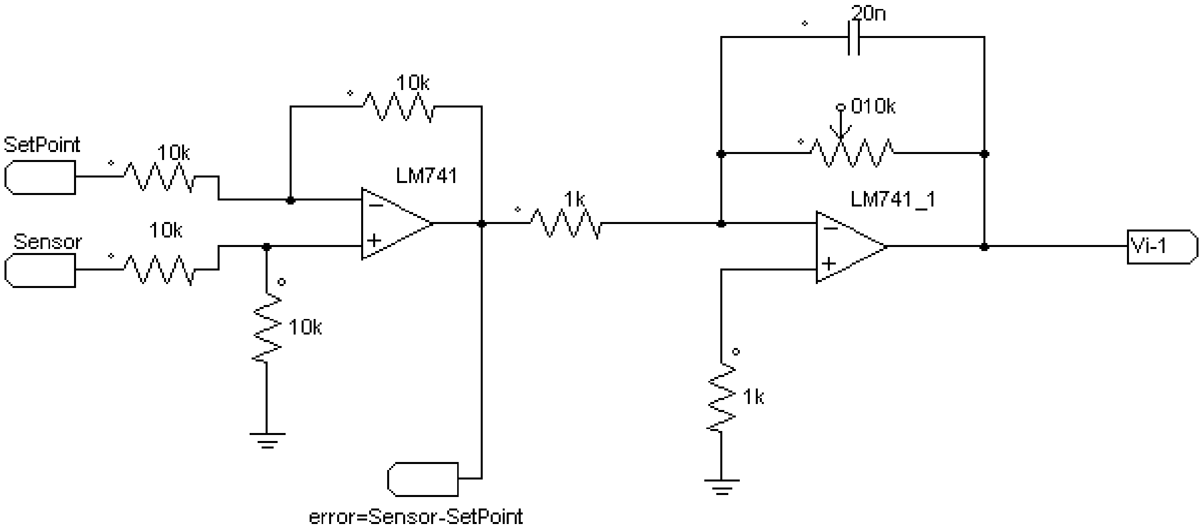

Figure 20 PI controller circuit

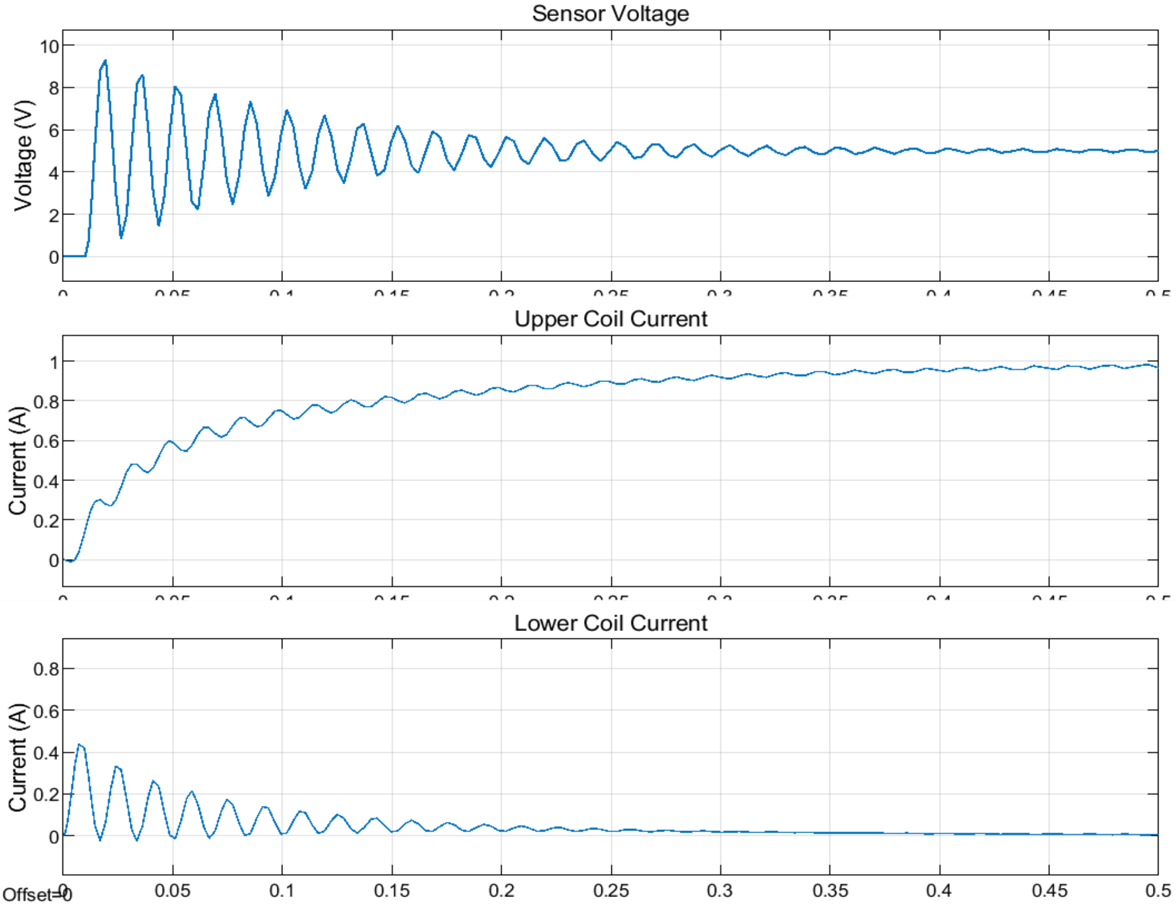

Figure 21 Shaft displacement and coils current

As can be seen in Figure (20), the sensor output was applied as input to the circuit and compared to the reference voltage, calculating the error in the output of the first Op-amp. The gain (P) could be altered by altering resistance in the second Op-amp. The desired capacitance for the integral term is selected as 20 nF, and the variable resistance was set to 5 kΩ to obtain the desired output. It is worth noting that the controller output V_{i-1} would be connected to the input of the driver circuit (Figure (19)). Given that it is a first-order circuit, the time constant of the controller circuit can be calculated using the equation below:

$$\tau = R \cdot C = 5000 \times 20 \times 10^{-9} = 100 \times 10^{-6} sec$$

The cut off frequency of the circuit is calculated as:

$$f = \frac{1}{\tau} = \frac{1}{100 \times 10^{-6}} = 10kHz$$

Therefore, the control circuit was fast enough to ensure effective performance in the system. Figure (21) depicts the sensor's output voltage, which reveals shaft displacement and current in the upper and lower coils, as well as the controller's activity to reduce displacement.

4.8 Results and discussion

The proposed suspension system was validated by measuring ohmic resistance, capacitance, rotor displacement and motor stand acceleration at different speeds.

4.8.1 Measurement of ohmic resistance and capacitance

To validate suspension at different speeds, ohmic resistance between the rotor and the porous piece of the air bearing was measured using a KYORITSU KEW1008 multimeter. Figure (22) shows the resistance at different speeds.

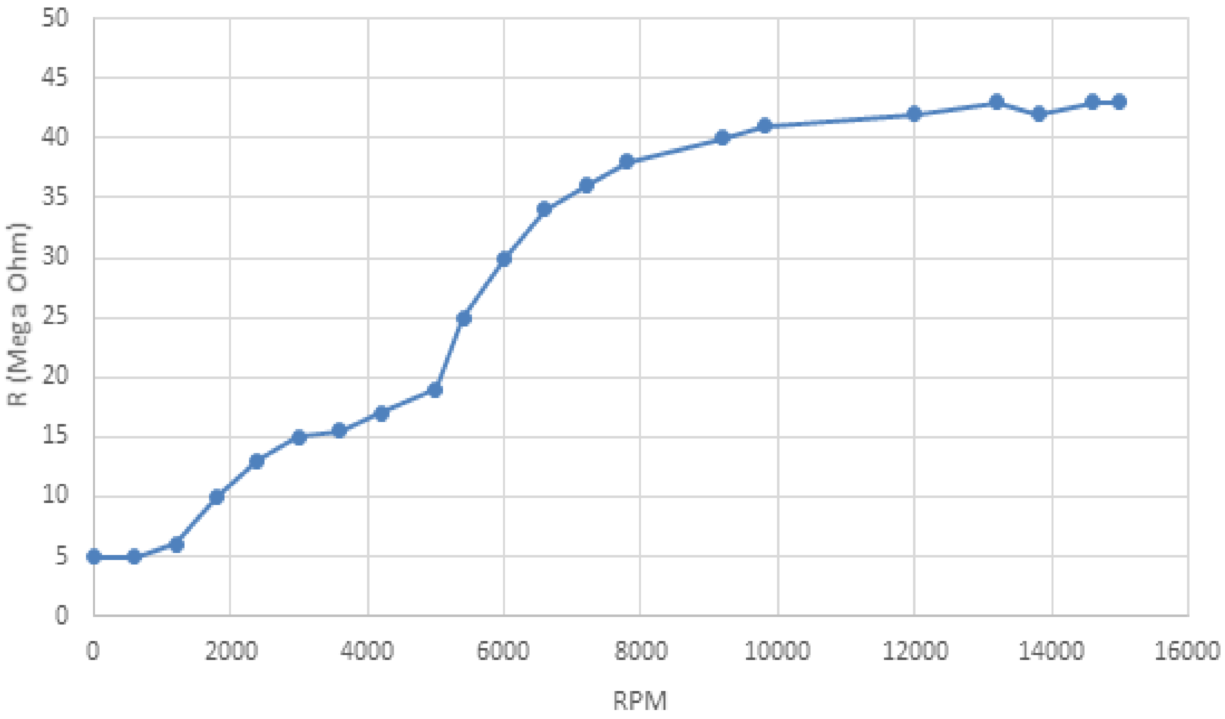

Figure 22 Ohmic resistance between the rotor and air bearing at different speeds

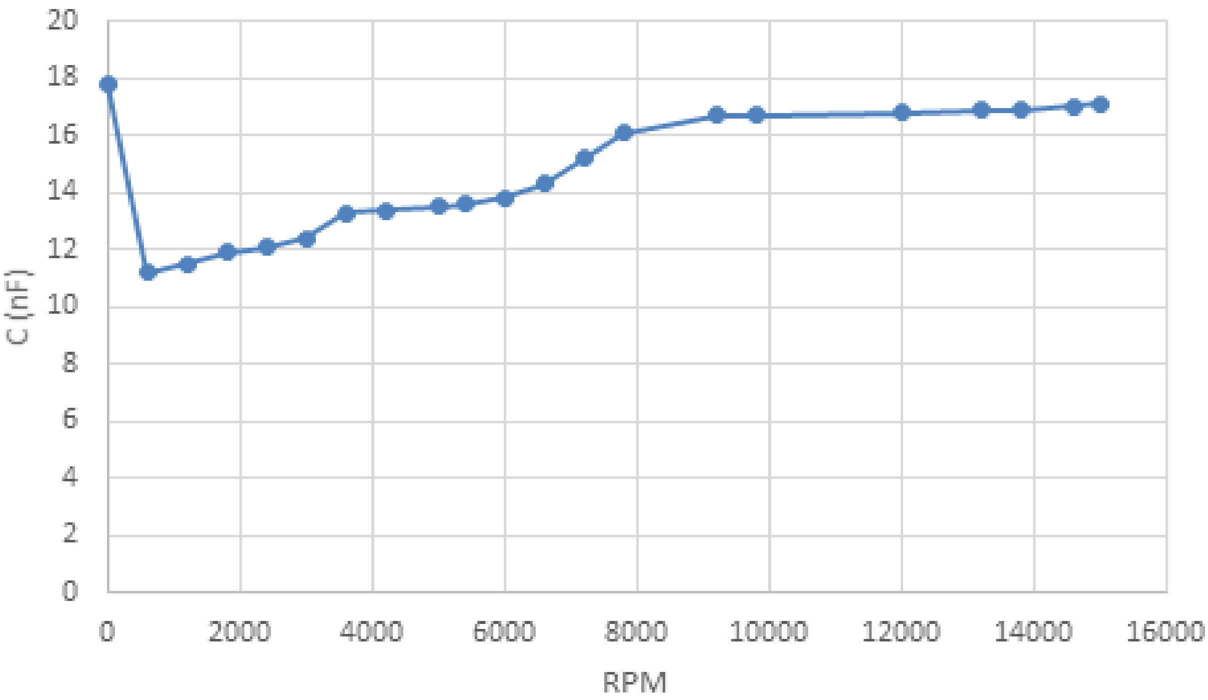

Figure 23 Capacitance between the rotor and air bearing at different speeds

Resistance is 5 MΩ at the speed of zero, shows the suspension in the air bearing system. It increased as the speed increased, reaching nearly 45 MΩ at a speed of 15,000 rpm. This is attributed to the increased air cushion stiffness upon shaft rotation. Due to shear stress, the air filled the entire gap between the rotor and the air bearing, increasing the air cushion stiffness. The capacitance between the rotor and air bearing was measured at different speeds, as shown in Figure (23) Capacitance was 18 nF at the speed of zero. It immediately dropped to 11 nF once the shaft began rotating. It increased to nearly 18 nF as the rotational speed increased. This implies that the dielectric constant of air may change upon a change in air cushion stiffness.

4.8.2. Displacement measurement of the rotor

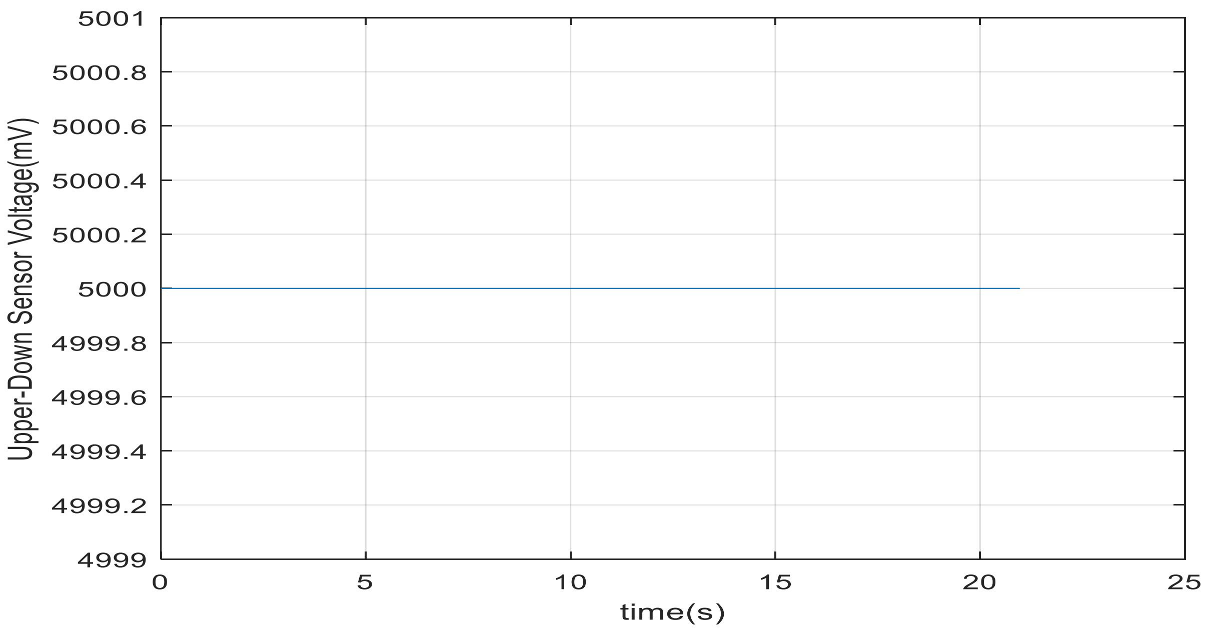

Figure 24 Top sensor output voltage for 20 s at 3000 rpm in the free run mode

When the VFD is connected to the motor (VFD is on), the switching frequency induces noise on the sensor's output. To eliminate VFD noise, it is required to speed up the motor to the intended speed and leave it to the free run mode. Signals are recorded after switching the VFD off. Figures (24) and (25) plot the sensor outputs.

As can be seen, the shaft rotated at the center at low speeds without vibration. At higher speeds, however, the shaft underwent slight vibrations. Figure (26) shows the output voltage of the sensors at 15,000 rpm.

As can be seen in Figure (26), the maximum voltage deviation is 50 mV, corresponding to a displacement of 2 μm.

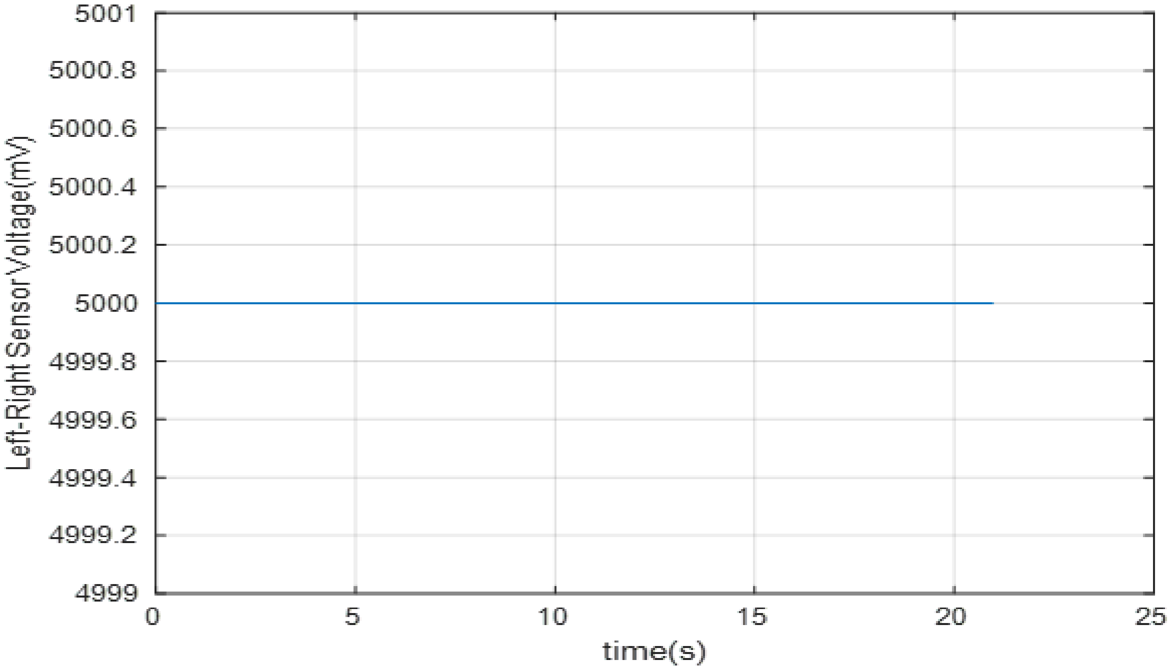

Figure 25 Right sensor output voltage for 20 s at 3000 rpm in the free run mode

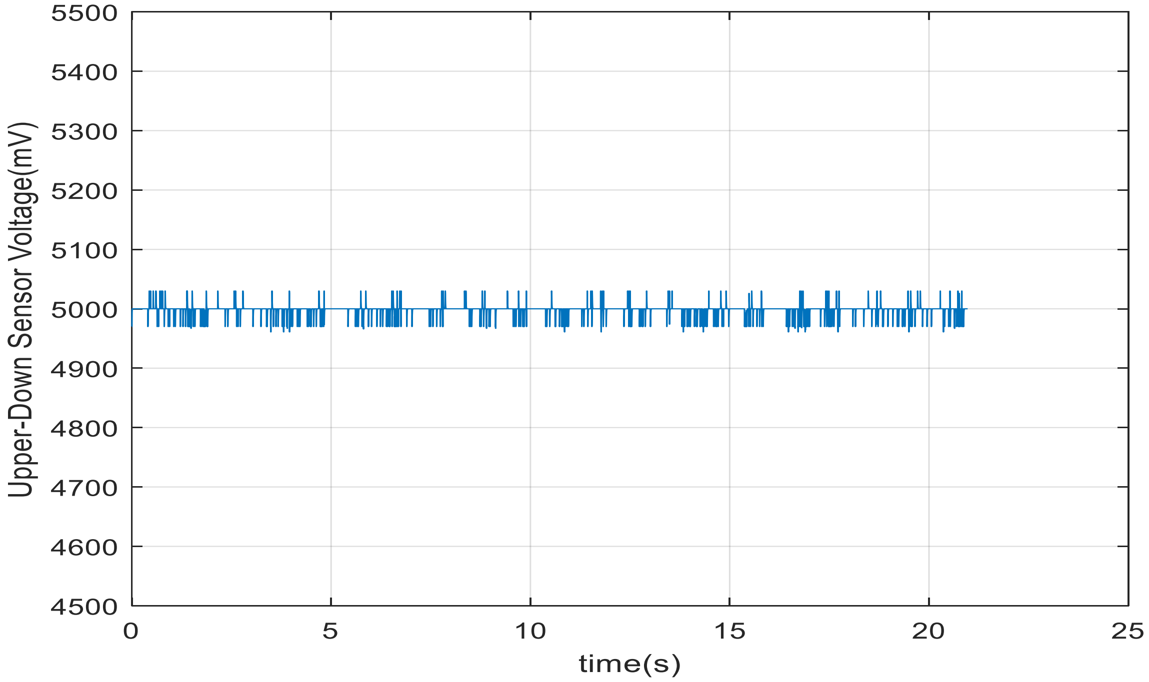

Figure 26 Top sensor output voltage for 20 s at 15,000 rpm in the free run mode

4.8.3 Acceleration measurement of the motor stand

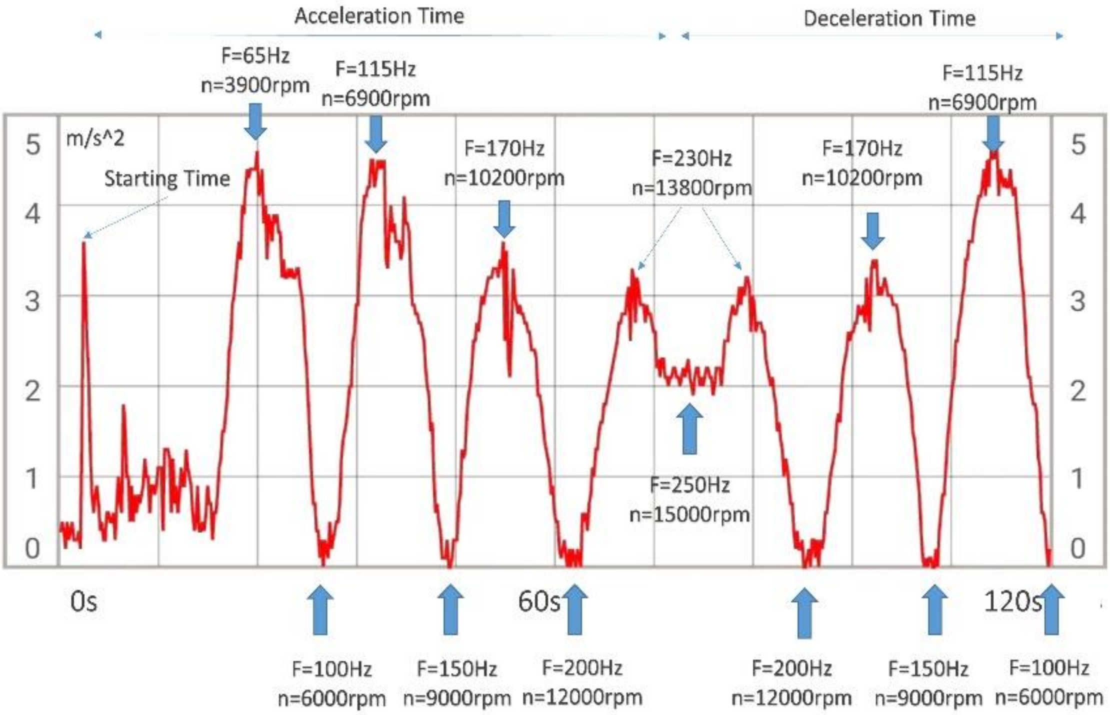

Figure 27 Accelerations of the motor stand at the speeds of 0 to 15.000 rpm

The speed of the induction motor is changed by adjusting the Variable Frequency Drive (VFD), and the acceleration of the motor stand is measured. It is important to note that accelerations are influenced by the type of motor electrical connection (Star or Delta) and the frequency switching of VFD. The motor was driven to 15,000 rpm and then decelerated using the braking mode of the VFD, and acceleration measured using an STMicro AGD3 accelerometer. The VFD switching frequency is 15kHz with a Delta electrical connection. Figure (27) depicts acceleration at 0-15,000 rpm and deceleration at 15000-6000 rpm. The VFD frequency was raised from 0 to 250 Hz, then decreased to 100 Hz.

5 Conclusion

This paper introduced a hybrid air-magnetic bearing system. Suspension performance and rotor displacement were assessed at various motor speeds. At speeds as high as 3000 rpm, the shaft displacement was almost negligible. It was discovered to be 2 μm at a speed of 15,000 rpm. The developed system allows for the use of air bearings independently up to 3000 rpm, while higher speeds need the employment of combined air and magnetic parts. Furthermore, the magnetic bearing cannot fulfill the suspension function without the presence of the air bearing. The system was tested at frequencies of up to 250 Hz or 15,000 rpm. Because of the aerodynamic effect, increasing the motor speed stiffened the air cushion and increased resistance between the rotor and the air bearing and at high speeds enhanced suspension stability and vibration damping. Also, the use of magnetic bearings at high speeds with appropriate control helps to dampen vibrations. Thus, the combination of air and magnetic bearings improves system reliability. The motor structure, VFD system, rotor, and bearing system all have an impact on speed enhancement. Future research could replace three-phase induction motors with brushless DC motors (BLDC) or turbine motors to increase speeds. Furthermore, a vertical system arrangement can be used to compensate for the shaft's gravitational influence and simplify the magnetic bearing control system.

6 Funding

The authors declare that no funds, grants, or other support were received during the preparation of this manuscript.

7 Conflict of interest

On behalf of all authors, the corresponding author states that there is no conflict of interest.

References

[1] R. Alimohamadi, "Improvement of Magnetic Bearing Operation for the Rotational Speed of 3000rpm," *M.Sc. Thesis*, Tarbiat Modares University, Tehran, Iran, 2009.

[2] T. Benšic, M. Barukcic, Ž. Hederic, V. Corluka, N. B. Raicevic, and I. Iatcheva, "Position Estimation of Active Magnetic Bearing Shaft using Auxiliary Coils," *COMPEL- The International Journal for Computation and Mathematics in Electrical and Electronic Engineering*, Vol. 37, No. 4, pp. 1328-1341, 2018, https://doi.org/10.1108/COMPEL-08-2017-0366.

[3] I. Cracaoanu, "Air Bearings in High Precision Systems," *Sustainable Construction and Design*, Vol. 4, 01/01 2013, https://doi.org/10.21825/scad.v4i2.1041.

[4] S. Dash, and K. S. Swarup, "Design Optimization of Single Axis Thrust Magnetic Bearing Actuator," *International Journal of Applied Electromagnetics and Mechanics*, Vol. 47, No. 3, pp. 661-680, 2015, https://doi.org/10.3233/JAE-140041.

[5] S. Greco, A. Lange, B. Kirsch, and J. C. Aurich, "Simulation-based Design of an Ultrasonic-assisted Air Bearing Spindle for Micro Machining," *Procedia CIRP*, Vol. 82, pp. 160-165, 2019, https://doi.org/10.1016/j.procir.2019.04.163.

[6] P. Imoberdorf, C. Zwyssig, S. D. Round, and J. W. Kolar, "Combined Radial-axial Magnetic Bearing for a 1 kW, 500,000 rpm Permanent Magnet Machine," in *APEC 07-Twenty-Second Annual IEEE Applied Power Electronics Conference and Exposition*, IEEE, 25 February 2007 - 01 March 2007, Anaheim, CA, USA, pp. 1434-1440, https://doi.org/10.1109/APEX.2007.357705.

[7] F. Ismagilov, V. Y. Vavilov, and V. Ayguzina, "Stability of Magnetic Bearings on Lorentz Forces," in *Journal of Physics: Conference Series*, 2018, Vol. 944, No. 1: IOP Publishing, p. 012042, https://doi.org/10.1088/1742-6596/944/1/012042.

[8] P. Samanta, N. Murmu, and M. Khonsari, "The Evolution of Foil Bearing Technology," *Tribology International*, Vol. 135, pp. 305-323, 2019, https://doi.org/10.1016/j.triboint.2019.03.021.

[9] M. S. Song, "Design and Experimental Study of Hydrostatic Thrust Air Foil Bearing," *M.Sc. Thesis*, Mechanical and Aerospace Engineering Thesis, Mechanical and Aerospace Engineering Department, University of Texas, Arlington, USA, 2018, https://books.google.com/books?id=6Hc9zwEACAAJ.

[10] G. Zywica and B. Paweł, "Investigation of Gas Foil Bearings with an Adaptive and Non-linear Structure," *Acta Mechanica et Automatica*, Vol. 13, No. 1, pp. 5-10, 03/01 2019, https://doi.org/10.2478/ama-2019-0001.

[11] S. I. Bekinal, S. S. Kulkarni, and S. Jana, "A Hybrid (Permanent Magnet and Foil) Bearing Set for Complete Passive Levitation of High-speed Rotors," *Proceedings of the Institution of Mechanical Engineers, Part C: Journal of Mechanical Engineering Science*, Vol. 231, No. 20, pp. 3679-3689, 2017, https://doi.org/10.1177/0954406216652647.

[12] Y. Li, "Study on the Characteristics of Hybrid Magnetic-gas Bearing of a Turbo Expander," Ph.D. Dissertation, University of Science and Technology Beijing, China, 2017.

[13] Q. Liu, L. Wang, and M. Feng, "Clearance Compatibility and Design Principle of the Single-structured Hybrid Gas-magnetic Bearing," *Industrial Lubrication and Tribology*, Vol. 75, No. 10, pp. 1219-1228, 2023, https://doi.org/10.1108/ILT-03-2023-0077.

[14] Q. Liu, L. Wang, Y. Li, and G. Lei, "Single-structured Hybrid Gas-magnetic Bearing and its Rotordynamic Performance," *Nonlinear Dynamics*, Vol. 104, pp. 333-348, 2021, https://doi.org/10.1007/s11071-021-06295-5.

[15] Q. Liu, L. Wang, S. Zhang, X. Wang, C. Yu, and G. Lei, "Quantitative Control of the Zero-bias-current Electromagnetic Bearings for Lower Power Consumption," *International Journal of Applied Electromagnetics and Mechanics*, Vol. 62, No. 2, pp. 221-242, 2020, https://doi.org/10.3233/JAE-180127.

[16] F. Zhao, C. A. Andersson, J. Singh, and C. Emmons, "Air Bearing Design Optimization," 2000, [Online], Available: https://api.semanticscholar.org/CorpusID:76650455.

[17] S. Gao, K. Cheng, S. Chen, H. Ding, and H. Fu, "Computational Design and Analysis of Aerostatic Journal Bearings with Application to Ultra-high Speed Spindles," *Proceedings of the Institution of Mechanical Engineers, Part C: Journal of Mechanical Engineering Science*, Vol. 231, pp. 1205 - 1220, 2017, https://doi.org/10.1177/0954406216639344.

[18] Q. Wu, Y. Sun, W. Chen, H. Liu, and X. Luo, "An Mechatronics Coupling Design Approach for Aerostatic Bearing Spindles," *International Journal of Precision Engineering and Manufacturing*, pp. 1-12, 2019, https://doi.org/10.1007/s12541-019-00098-w.

[19] A. Smirnov, N. Uzhegov, T. Sillanpää, J. J. Pyrhönen, and O. Pyrhönen, "High-speed Electrical Machine with Active Magnetic Bearing System Optimization," *IEEE Transactions on Industrial Electronics*, Vol. 64, pp. 9876-9885, 2017, https://doi.org/10.1109/TIE.2017.2716875.

[20] R. I. Yamamoto, O. Horikawa, and I. da Silva, "Magnetic Bearing with Uniaxial Control using Magnetic, Electrodynamic and Electromagnetic Levitation," 2014, [Online]. Available: https://abcm.org.br/upload/files/PI_VII_01(1).pdf.

[21] Z. Huang, C. Li, Z. Zhou, B. Liu, Y. Zhang, M. Yang, T. Gao, M. Liu, N. Zhang, S. Sharma, Y. Suleiman Dambatta and Y. Li, "Magnetic Bearing: Structure, Model, and Control Strategy," *The International Journal of Advanced Manufacturing Technology*, Vol. 131, No. 5, pp. 3287-3333, 2024, https://doi.org/10.1007/s00170-023-12389-8.

[22] H. Heshmat, and D. S. Xu, "Experimental Investigation of 150 mm Diameter Large Hybrid Foil/Magnetic Bearing," in *Proceedings of the International Gas Turbine Congress*, 2003: Citeseer, pp. 2-7. [Online]. Available: https://citeseerx.ist.psu.edu/document?repid=rep1&type=pdf&doi=32293d25a9deba153e4b026642aa0cc3eef7a12f.

[23] H.-D. Jang, J. Kim, D.-C. Han, D.-Y. Jang, and H.-J. Ahn, "Improvement of High-speed Stability of an Aerostatic Bearing-rotor System using an Active Magnetic Bearing," *International Journal of Precision Engineering and Manufacturing*, Vol. 15, pp. 2565-2572, 2014, https://doi.org/10.1007/s12541-014-0628-y.

[24] Q. Liu, S. Zhang, Y. Li, G. Lei, and L. Wang, "Hybrid Gas-magnetic Bearings: An Overview," *International Journal of Applied Electromagnetics and Mechanics,* Vol. 66, No. 2, pp. 313-338, 2021, https://doi.org/10.3233/JAE-201579.

[25] M. M. Sheikhi, "Dynamic Analysis of Magnetic Bearing and Fabrication of a Laboratory Sample," *Ph.D. Thesis*, Tarbiat Modares University, Tehran, Iran, 2008.

[26] Y. Hojjat, M. M. Sheikhi, H. . Mosavi. Hondori, and R. Alimohamadi, "Design and Manufacturing of an Active Magnetic Bearing," (in English), *Modares Mechanical Engineering*, Vol. 9, No. 1, pp. 153-160, 2009, [Online], Available: http://mme.modares.ac.ir/article-15-9175-en.html.

Nomenclature

English symbols

A	Air gap cross sectional area
A_{fe}	Core cross sectional area
B	Magnetic flux density
F	Electromagnetic force
f	Frequency
g	Air gap
i	Coil current
l_{fe}	Average magnetic path length
N	Number of turns

Greek symbols

Φ	Magnetic flux
$\mathscr{F}$	Magnetomotive force
$\mathscr{R}$	Reluctance
μ_0	Air permeability coefficient ($4\pi\times10^{-7}$)
μ_r	Relative permeability coefficient
τ	Time constant

Abbreviations

PTFE	Polytetrafluoroethylene
VFD	Variable Frequency Drive